

## X-RAY EMISSION FROM THE WOLF-RAYET BUBBLE NGC 6888 I. CHANDRA ACIS-S OBSERVATIONS

J. A. TOALÁ<sup>1</sup>, M. A. GUERRERO<sup>1</sup>, R. A. GRUENDL<sup>2</sup>, AND Y.-H. CHU<sup>2</sup>

<sup>1</sup>Instituto de Astrofísica de Andalucía, IAA-CSIC, Glorieta de la Astronomía s/n, 18008 Granada, Spain

<sup>2</sup>Department of Astronomy, University of Illinois, 1002 West Green Street, Urbana, IL 61801, US

*Draft version September 1, 2018*

### ABSTRACT

We analyze *Chandra* observations of the Wolf-Rayet (WR) bubble NGC 6888. This WR bubble presents similar spectral and morphological X-ray characteristics to those of S308, the only other WR bubble also showing X-ray emission. The observed spectrum is soft, peaking at the N VII line emission at 0.5 keV with additional line emission at 0.7–0.9 keV and a weak tail of harder emission up to  $\sim 1.5$  keV. This spectrum can be described by a two-temperature optically thin plasma emission model ( $T_1 \sim 1.4 \times 10^6$  K,  $T_2 \sim 7.4 \times 10^6$  K). We confirm the results of previous X-ray observations that no noticeable temperature variations are detected in the nebula. The X-ray-emitting plasma is distributed in three apparent morphological components: two caps along the tips of the major axis and an extra contribution toward the northwest blowout not reported in previous analysis of the X-ray emission toward this WR nebula. Using the plasma model fits of the *Chandra* ACIS spectra for the physical properties of the hot gas and the *ROSAT* PSPC image to account for the incomplete coverage of *Chandra* observations, we estimate a luminosity of  $L_X = (7.7 \pm 0.1) \times 10^{33}$  erg s<sup>-1</sup> for NGC 6888 at a distance of 1.26 kpc. The average rms electron density of the X-ray-emitting gas is  $\gtrsim 0.4$  cm<sup>-3</sup> for a total mass  $\gtrsim 1.2M_\odot$ .

*Subject headings:* ISM: bubbles – ISM: individual (NGC 6888) – stars: winds, outflows – stars: Wolf-Rayet – X-rays: individual (NGC 6888)

### 1. INTRODUCTION

Wolf-Rayet (WR) bubbles are expected to be filled with hot plasma at temperatures of  $\sim 10^7$ – $10^8$  K, but previous X-ray observations of hot bubbles have shown that this plasma presents lower temperatures, of the order of  $\sim 10^6$  K (see Chu 2008). The scarcity of X-ray detections among WR nebulae is also intriguing; there are only two WR nebulae detected in diffuse X-rays: S308 and NGC 6888 (Bochkarev 1988; Wrigge et al. 1994, 1998; Wrigge 1999; Wrigge & Wendker 2002; Chu et al. 2003; Wrigge et al. 2005; Zhekov & Park 2011; Toalá et al. 2012). These two WR bubbles share several characteristics: the X-ray-emitting plasma is confined inside optical shells where the H $\alpha$  emission presents a clumpy distribution inside an [O III] shell (Gruendl et al. 2000), and both bubbles are nitrogen-rich and surround WN stars with terminal wind velocities of  $\sim 1800$  km s<sup>-1</sup> (van der Hucht 2001). This configuration can be pictured as the WR wind sweeping up the previously ejected Red Supergiant (RSG) wind material whilst the central star photoionizing this material.

NGC 6888 has been the subject of many studies over the years since it was first reported by Sharpless (1959) and associated to its central WR star, WR 136, by Johnson & Hogg (1965). The most recent optical study of this nebula, presented by Fernández-Martín et al. (2012), investigated the ionization, chemical composition, and kinematics in several regions within the nebula. They concluded that NGC 6888 is composed by multiple shells, and its morphology can be interpreted as a sphere with an ellipsoidal cavity inside.

The first map of the diffuse X-ray-emitting gas in

NGC 6888 was presented by Bochkarev (1988) using *Einstein* observations; a total flux of  $\sim 10^{-12}$  erg cm<sup>-2</sup> s<sup>-1</sup> was detected in the 0.2–3.0 keV band. Wrigge et al. (1994) analyzed *ROSAT* PSPC observations and found a flux of  $(1.2 \pm 0.5) \times 10^{-12}$  erg cm<sup>-2</sup> s<sup>-1</sup>. Wrigge et al. (2005) made use of the *ASCA* SIS and *ROSAT* PSPC observations to fit a two-temperature model ( $T_1 \sim 1.3 \times 10^6$  K,  $T_2 \sim 8.5 \times 10^6$  K) and measured a total observed flux of  $\sim 10^{-12}$  erg cm<sup>-2</sup> s<sup>-1</sup>. The most recent X-ray observations of NGC 6888 are those obtained by Zhekov & Park (2011) using the *Suzaku* satellite. They concluded that the spectrum indicates a relatively cool plasma with  $T < 5 \times 10^6$  K and a small contribution from a much hotter plasma component with temperature greater than  $2 \times 10^7$  K. No appreciable temperature variations are found between the northern and southern regions of the nebula. The observed flux was reported to be  $2 \times 10^{-12}$  erg cm<sup>-2</sup> s<sup>-1</sup> in the 0.3–1.5 keV energy range.

In this paper we present *Chandra* observations of NGC 6888. A preliminary analysis of this dataset was presented by Chu et al. (2006), where they showed the diffuse X-ray emission coming from the NE quadrant of the nebula (ACIS-S CCDS3). Here we present the analysis of the ACIS-S CCDS3 and CCDS4, covering  $\sim 62\%$  of the nebula. The spectral properties of the X-ray-emitting plasma are compared to those derived previously by other authors using observations obtained by other X-ray facilities. The data from CCDS4 show an additional spatial component of X-ray emission which has not been reported in previous observations.

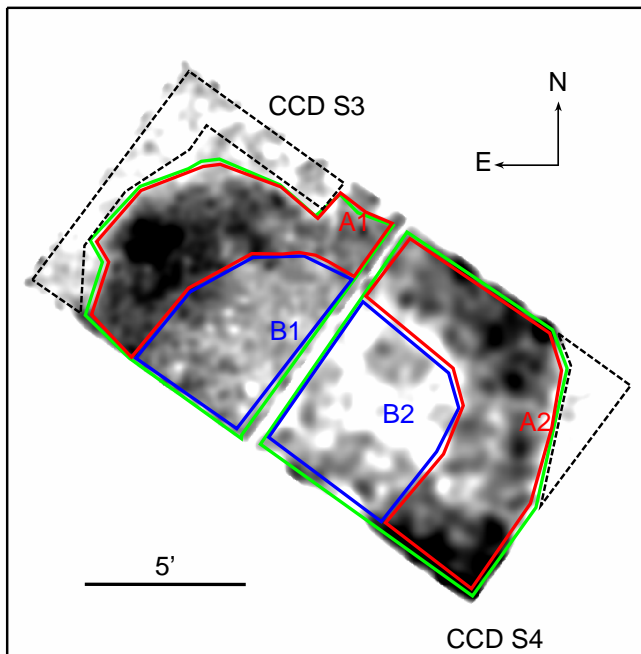


FIG. 1.— *Chandra* ACIS-S image of the diffuse X-ray emission of NGC 6888 in the 0.3-2.0 keV band. Point sources have been excised from this image. The regions used for spectral analysis are indicated with polygonal apertures: green, red, and blue solid lines correspond to source regions, and black dashed lines to background regions.

## 2. CHANDRA OBSERVATIONS

The superb angular resolution and sensitivity at soft energies of *Chandra*, as compared to previous satellites that have observed NGC 6888, allow a more reliable study of the soft X-ray emission from the hot plasma in this nebula. The *Chandra* observation of NGC 6888 was performed on 2003 February 19-20 (Observation ID 3763; PI: R.A. Gruendl) using the Advanced CCD Imaging Spectrometer (ACIS-S) for a total exposure time of 92.8 ks. The NE quadrant of NGC 6888 was imaged on the back-illuminated ACIS-S CCD S3 while the western region was imaged by CCD S4. The *Chandra* Interactive Analysis of Observations (CIAO) software package version 4.4 was used to analyze the data using CALDB version 3.2.2. Very short periods of high background affected the data and the resulting useful exposure time is 88.0 ks after excising dead time periods. The *Chandra* ACIS-S observation detects diffuse emission from NGC 6888 in the soft energy band below 2.0 keV. No significant emission is detected above this energy limit. The total background-subtracted count rates of the diffuse X-ray emission for CCD S3 and CCD S4 are 0.160 and 0.053 cnts s<sup>-1</sup>, respectively.

## 3. SPATIAL DISTRIBUTION OF THE DIFFUSE X-RAY EMISSION

In order to analyze the spatial distribution of the hot gas in NGC 6888, we excised all point sources from the observation using the CIAO *dmfilth* routine. The identification of the point sources was made using the CIAO *wandetect* routine. The image of the diffuse X-ray emission was extracted in the 0.3-2.0 keV energy band and smoothed with the CIAO task *csmooth*, with a Gaussian

kernel of 4'' in the brightest regions and 16'' and 24'' in the faintest ones for the CCD S3 and S4, respectively. The resultant image is shown in Figure 1.

We compare in Figure 2-left the X-ray image with H $\alpha$  and [O III] optical images of the nebula taken with the 1 m telescope at the Mount Laguna Observatory (Gruendl et al. 2000). This figure shows a limb-brightened spatial distribution of the X-ray emission confined within the optical [O III] shell. In particular the X-ray-emitting gas in the NE region of the nebula (ACIS-S CCD S3) seems to fill all the area within the nebula with a broad emission peak superposed on the H $\alpha$  clumps, while the emission detected in ACIS-S CCD S4 can be associated with the southwest cap of the nebula, and with emission outside the H $\alpha$  shell but inside the western [O III] skin.

For comparison, we also present in Figure 2-right a composite picture of the same optical images and the X-ray emission detected by *ROSAT* PSPC (Wrigge et al. 1994, 2005). This image demonstrates that the X-ray emission from NGC 6888 is stronger at the caps along the major axis, but an extra contribution can be detected at the westernmost regions of the nebula, just inside the optical [O III] shell. This additional spatial component of X-ray emission, hinted in previous images of the nebula made with *ROSAT* HRI and *ASCA* (Wrigge et al. 1994; Wrigge & Wendker 2002; Wrigge et al. 2005), is reminiscent of the Northwest blowout in S 308 (Chu et al. 2003; Toalá et al. 2012).

## 4. PHYSICAL PROPERTIES OF THE HOT GAS IN NGC 6888

We have carried out the study of the hot gas of NGC 6888 in several steps. First, we have studied the emission from the nebular gas detected in CCD S3 and CCD S4, keeping in mind that the former has more reliable spectral resolution and sensitivity at lower energies than CCD S4. Therefore, we have defined two regions encompassing the diffuse X-ray emission registered in the field of view of the *Chandra* ACIS-S CCD S3 and S4 (green polygonal lines in Figure 1).

For further analysis, we have defined several smaller polygonal aperture regions, also shown in Figure 1, corresponding to different features presented in NGC 6888: regions labeled as A comprise the apparent shell and caps, and regions labeled with B correspond to the shell interior. We note that both regions are present within each CCD detector, and thus we have extracted two spectra corresponding to each morphological feature. For example, A1 corresponds to a region extracted from CCD S3 and A2 to a region extracted from CCD S4. The same applies to regions B1 and B2.

### 4.1. Spectral Properties

As discussed in Toalá et al. (2012), the extraction of spectra from extended sources, as is the case of WR bubbles, is challenging because the emission fills almost the entire field of view of the instrument. The background contribution can be estimated from high signal-to-noise blank fields, but as mentioned by Toalá et al. (2012), this technique does not produce suitable results because WR bubbles are located in regions close to the Galactic Plane where extinction and background emission are significant (Snowden et al. 1997). To show the contribution of the Galactic background, we plot in Figure 3 the

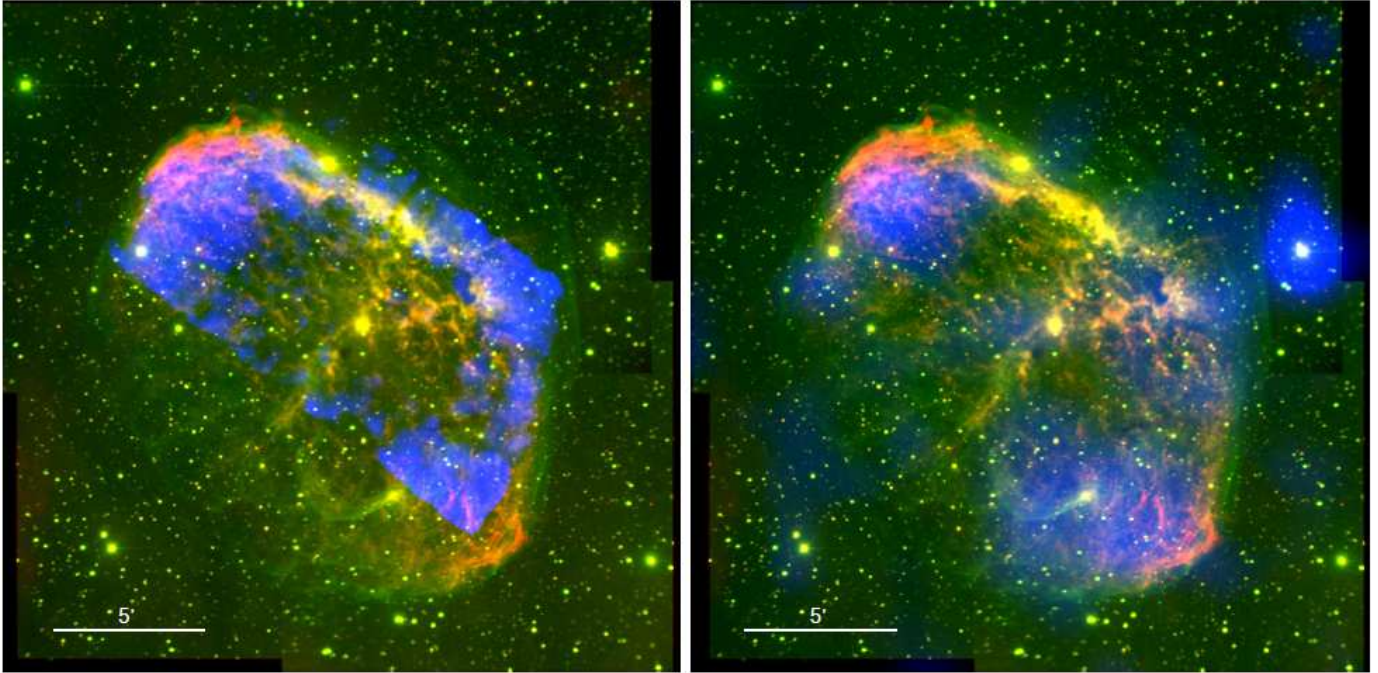


FIG. 2.— Left: Composite color picture of the *Chandra* ACIS-S observation of NGC 6888 (blue) and MLO H $\alpha$  (red) and [O III] (green) images. Right: Same as in *left* image but with *ROSAT* PSPC image (blue). North is up, East to the left.

background-unsubtracted spectrum from CCD S3 and a background spectrum extracted from the edge of the camera. X-ray emission from the background is soft and show lines in the 0.3–1.0 keV energy band from thermal components (see also figure 5 in Toalá et al. 2012, for the case of S 308). The spectral shape of the background emission certainly differs from that derived from ACIS blank-field observations. Therefore, the most feasible procedure to subtract the background contribution is the use of background spectra extracted from areas near the camera edges, even though the instrumental responses for sources and background regions do not completely match each other.

The individual background-subtracted spectra of the diffuse emission of the NE quadrant and western region of NGC 6888 (namely CCD S3 and CCD S4) are presented in Figure 4, as well as the individual spectra extracted from regions A1, A2, B1, and B2. All spectra were extracted using the CIAO task *specextract*, which generates the source and background spectra and their corresponding calibration files. The most notable differences in the spectral shapes are attributed to the differences in sensitivity of the ACIS-S CCD S3 and CCD S4. All spectra are soft and show two main peaks, a narrow peak at 0.5 keV and a broader peak around 0.7–0.9 keV. The feature around 0.5 keV can be identified with the N VII ion, while the feature around  $\sim$ 0.7–0.9 keV can be associated with the Fe complex and Ne lines. Above 1.0 keV, the emission declines and diminishes at energies  $\simeq$ 1.5 keV. We note that the spectra extracted from CCD S4 show the instrumental Au M complex at 2.2 keV, which has not been properly removed due to the reduced spatial extent of the background region.

In accordance with the spectral properties and previous spectral fits, all X-ray spectra from NGC 6888 have been fit with XSPEC v12.7.0 (Arnaud 1996) us-

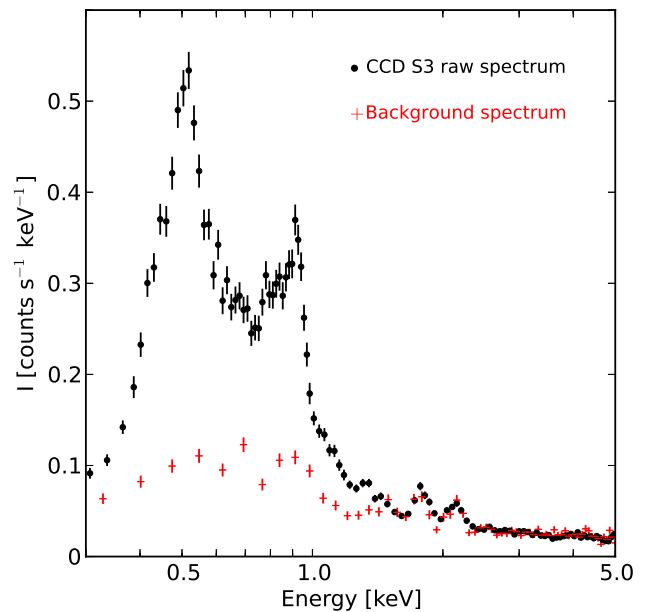


FIG. 3.— Comparison of the raw CCD S3 spectrum (black circles) and scaled background spectrum extracted from the edges of CCD S3 (red crosses). The emission lines around 2 keV in the background spectrum are instrumental lines.

ing an absorbed two-temperature *apec* optically thin plasma emission model with an absorption model using Balucińska-Church & McCammon (1992) cross-sections. A low temperature component is used to model the bulk of the X-ray emission, while a high temperature component is added to model the extra emission at and

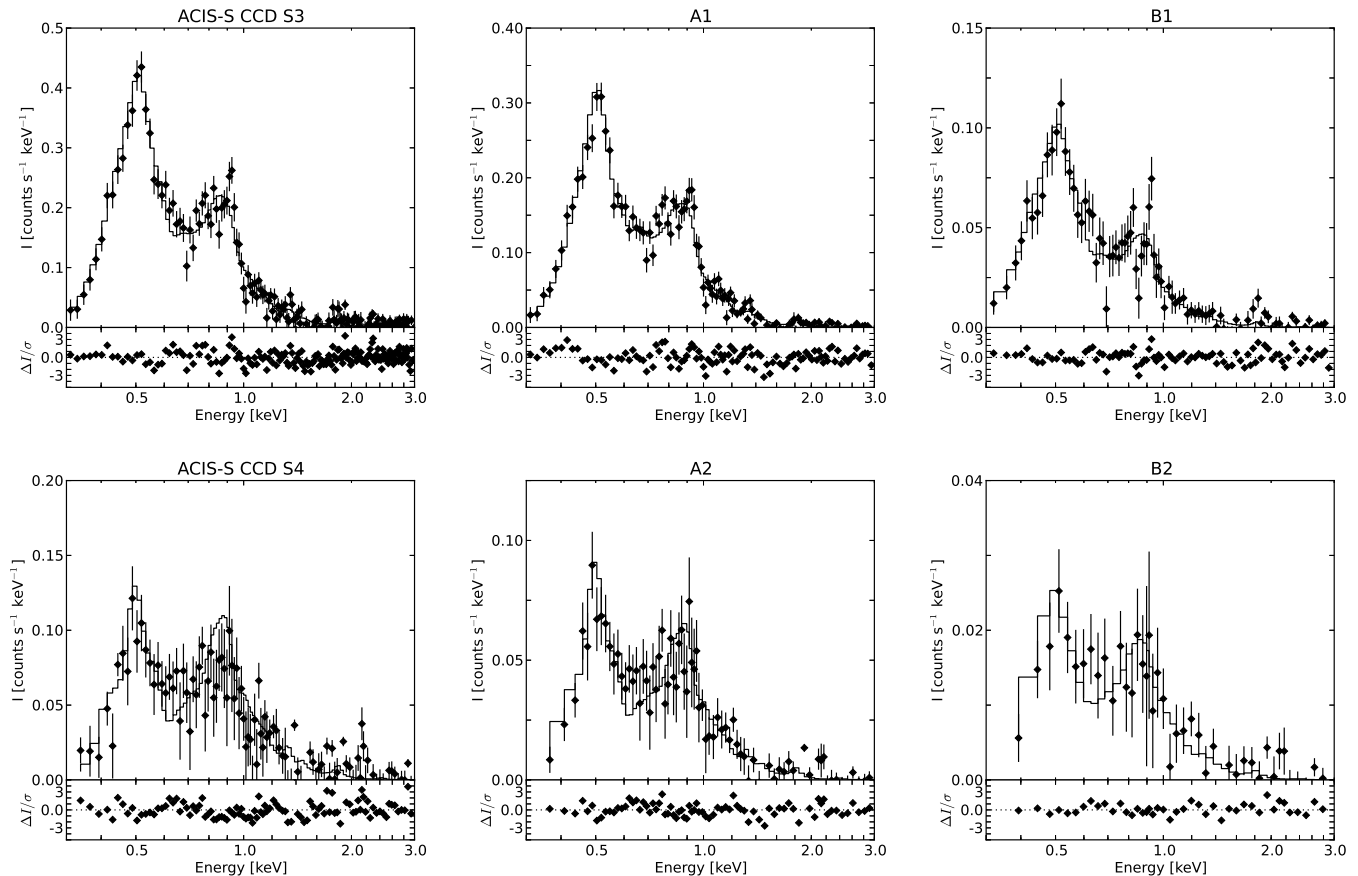


FIG. 4.— Background-subtracted *Chandra* ACIS-S spectra of the NE (top panels) and western (bottom panels) regions of NGC 6888 over-plotted with their best-fit two-temperature *apec* model (solid lines) in the energy range of 0.3 – 3 keV.

above  $\sim 0.7$  keV. As in previous studies of the X-ray emission from WR bubbles (see Chu et al. 2003; Zhekov & Park 2011; Toalá et al. 2012), we have initially adopted nebular abundances for the X-ray-emitting plasma. In particular, we have used abundance values for N, O, and Ne of 3.2, 0.41, and 0.85 times the solar values (Anders & Grevesse 1989) as averaged from regions X1 and X2 described in Fernández-Martín et al. (2012, see their Table 4), and 0.39 times the solar value for S (Moore et al. 2000). Models with variable C, Mg, Fe, and Ne abundances were also tested. We found that the fitted abundances of Mg and Fe converged to solar values, whereas those of Ne tended to 0.85 times the solar value, i.e., the value determined from optical spectrophotometry (Fernández-Martín et al. 2012). Consequently, we decided to fix the abundances of Mg, Fe, and Ne to these values. As for the carbon abundance, the fits could not converge to specific values because the C VI line at 0.37 keV or C V triplet at 0.3 keV are in the low energy range, where absorption is high and the instrument sensitivity is low. Therefore, we fixed the value of the carbon abundance to its solar value. Finally, all spectra were modeled with varying nitrogen abundance ( $X_N$ ) as the prominent N VII line at 0.5 keV seems to suggest a possible nitrogen enrichment of the X-ray-emitting plasma.

The simulated two-temperature *apec* model spectra obtained were absorbed by the interstellar hydrogen column of  $3.13 \times 10^{21} \text{ cm}^{-2}$  implied by optical measure-

ments (Hamann et al. 1994). This is the same value used by previous authors (Wrigge et al. 1994, 2005) which was found to be uniform throughout NGC 6888 by Wendker et al. (1975). Models with variable columnar density  $N_H$  were also attempted. The absorption column density showed a correlation with the temperature of the main plasma component ( $T_1$ ), with values  $2\text{--}4 \times 10^{21} \text{ cm}^{-2}$  which is adopted here and is consistent with the value used by Zhekov & Park (2011).

The resultant model spectra were compared with the observed spectra in the 0.3 - 3 keV energy range and the  $\chi^2$  statistics was used to determine the best-fit models. A minimum of 60 counts per bin was required for the spectral fit. The plasma temperatures ( $kT_1$ ,  $kT_2$ ) with  $1\sigma$  uncertainties, normalization factors<sup>1</sup> ( $A_1$ ,  $A_2$ ), and nitrogen abundance ( $X_N$ ) of the best-fit models are listed in Table 1. Fluxes and luminosities listed in this table have been computed for the energy range 0.3-2.0 keV. The best-fit models are over-plotted on the background-subtracted spectra, together with the residuals of the fits as solid lines in Figure 4.

#### 4.1.1. Properties of the NE X-ray Emission

The parameters of the best-fit model of the NE quadrant of NGC 6888 are listed in Table 1 as CCD S3.

<sup>1</sup>  $A = 1 \times 10^{-14} \int n_e n_H dV / 4\pi d^2$ , where  $d$  is the distance,  $n_e$  is the electron density, and  $V$  the volume in cgs units.



The model presents a low-temperature component of  $1.6 \times 10^6$  K and a second component of  $7.8 \times 10^6$  K with an observed flux ratio,  $f_1/f_2 \sim 3$ , corresponding to an intrinsic flux ratio  $F_1/F_2 \sim 14$ . The total observed flux in the 0.3–2 keV energy band is  $(6.4^{+0.1}_{-0.2}) \times 10^{-13}$  erg cm $^{-2}$  s $^{-1}$  while the total unabsorbed flux is  $(8.0^{+0.4}_{-0.2}) \times 10^{-12}$  erg cm $^{-2}$  s $^{-1}$ . The nitrogen abundance of the best-fit model is  $\approx 5.3$  times that of the solar value.

In the case of the resultant spectra from regions A1 and B1, the temperatures are consistent with those obtained from the whole region,  $T_1 = 1.6 \times 10^6$  K and  $T_2 = 7.9 \times 10^6$  K for region A1, and  $T_1 = 1.4 \times 10^6$  K and  $T_2 = 7.7 \times 10^6$  K for region B1, respectively. Their nitrogen abundances are 5.3 and 3.7 times the solar value for A1 and B1, respectively.

#### 4.1.2. Properties of the Western X-ray Emission

The background-subtracted X-ray spectra from the western regions of NGC 6888 are shown in the lower panels of Figure 4, which correspond to the total diffuse emission detected by the CCDS4 (left), the emission from the rim registered by region A2 (middle), and the emission from inside the WR nebula registered by region B2 (right). The parameters of the best-fit models over-plotted to these spectra are presented in Table 1. We remark that the fits of these spectra failed to constrain accurately the nitrogen abundance<sup>2</sup>, and therefore we fixed its value to that found for the spectrum of the CCDS3.

The model of the X-ray-emitting plasma detected in the western regions of NGC 6888 (the ACIS CCDS4 spectrum) has a lower dominant temperature of  $1.2 \times 10^6$  K with a second component of  $7.4 \times 10^6$  K. The total observed flux is  $(8.8 \pm 0.8) \times 10^{-13}$  erg cm $^{-2}$  s $^{-1}$ , while the unabsorbed flux is  $(1.5 \pm 0.3) \times 10^{-11}$  erg cm $^{-2}$  s $^{-1}$ , with an unabsorbed flux ratio of  $F_1/F_2 \sim 31$ .

The resultant spectra from A2 and B2 are consistent from that obtained for the total spectrum extracted from CCDS4.  $T_1 = 1.2 \times 10^6$  K and  $T_2 = 7.4 \times 10^6$  K for region A2, and  $T_1 = 1.4 \times 10^6$  K and  $T_2 = 7.5 \times 10^6$  K for region B2<sup>3</sup>. The unabsorbed flux ratios are  $F_1/F_2 \sim 35$  and  $\sim 26$  for A2 and B2, respectively.

#### 4.2. Global Properties of the hot gas in NGC 6888

To assess the global properties of the hot gas in NGC 6888, we have derived the parameters of the two-temperature plasma emission model that best describes the total X-ray emission detected by *Chandra*. The

<sup>2</sup> At first glance, this may seem perplexing because the CCDS4 and B2 spectra have larger total count numbers than the B1 spectrum from CCDS3 which could be used instead to derive the nitrogen abundance. The cause of this apparent conflict originates in the reduced sensitivity of the front-illuminated (FI) CCDS4 at  $\sim 0.5$  keV, the energy of the N VII line, which is a few times smaller than that of the back-illuminated (BI) CCDS3. This is clearly illustrated by the differing shapes of the spectra detected by the BI CCDS3 and the FI CCDS4 (Figure 4). As a result, the FI CCDS4 detects a count number at the N VII line which is insufficient for a reliable estimate of the nitrogen abundance.

<sup>3</sup> Due to the low count number of the B2 spectrum, the temperature of the hottest component in this region could not be fitted. Consequently, the temperature of this component was fixed at 0.65 keV.

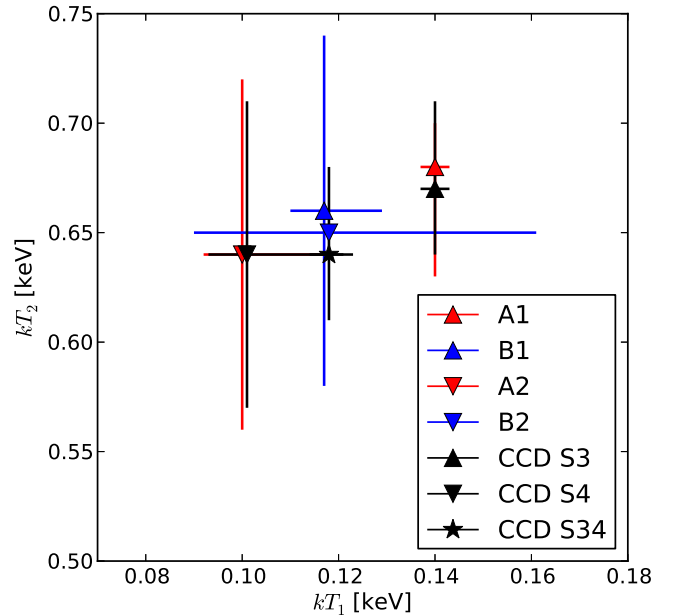


FIG. 5.— Plot of the temperatures of the cold and hot plasma components for the different spatial regions defined for the analysis of NGC 6888. The inset shows a chart of the correspondence between symbols and spatial regions, where the star marks the location of the temperatures derived from the joint fit CCD S34.

CCDS3 and CCDS4 spectra have been fitted simultaneously using the same hydrogen column density and plasma parameters ( $kT_1$ ,  $kT_2$ ,  $X_N$ ). The results of this joint fit are given in Table 1 as CCD S34. The normalization factor of the cold thermal component of both spectra ( $A_1^{S3}$ ,  $A_1^{S4}$ ) were obviously allowed to vary to account for the different volume emission measure of hot gas mapped by each detector. The ratio between the normalization factors of the cold and hot components was also allowed to vary, but it was kept the same for both spectra ( $A_2^{S3}/A_1^{S3} \equiv A_2^{S4}/A_1^{S4} \equiv A_2^{S34}/A_1^{S34}$ ), i.e., it was assumed that the relative contribution of both components of the X-ray-emitting plasma is the same across the nebula. The values of the normalization factors listed for this fit have been obtained by adding the normalization factor of each component for the CCD S3 and CCD S4 spectra ( $A_1^{S34} = A_1^{S3} + A_1^{S4}$ ,  $A_2^{S34} = A_2^{S3} + A_2^{S4}$ ). The temperature of the two components of this model,  $T_1 = 1.4 \times 10^6$  K and  $T_2 = 7.4 \times 10^6$  K, are enclosed within those obtained for the CCDS3 and S4 spectra. For comparison with all regions, we show in Figure 5 the temperature distribution obtained from our fits for the different regions. Accounting for the uncertainties, there is a good agreement for the temperature components of the different regions.

The total observed flux is  $f_X = (1.5 \pm 0.2) \times 10^{-12}$  erg cm $^{-2}$  s $^{-1}$ , which corresponds to an unabsorbed flux of  $F_X = (2.5 \pm 0.3) \times 10^{-11}$  erg cm $^{-2}$  s $^{-1}$ . The comparison between *ROSAT* PSPC and *Chandra* ACIS images indicates that the latter includes  $\simeq 62$  % of the total X-ray flux of NGC 6888. With this we can estimate a total X-ray intrinsic flux of  $F_{X,TOT} = (4.05 \pm 0.5) \times 10^{-11}$  erg cm $^{-2}$  s $^{-1}$ . Adopting a distance of 1.26 kpc,

the total X-ray luminosity of NGC 6888 in the 0.3-2.0 keV energy range is  $L_X = (7.7 \pm 0.1) \times 10^{33}$  erg s $^{-1}$ .

To proceed to the calculation of the electron density and mass of the X-ray-emitting plasma in NGC 6888 we need to adopt a geometrical model for the nebula in order to estimate the volume occupied by the hot plasma. It is tempting to assume an ellipsoidal geometry, as suggested by the H $\alpha$  images, however the *Chandra* ACIS-S and *ROSAT* PSPC observations of NGC 6888 have disclosed emission external to the H $\alpha$  shell, just inside the [O III] skin (see Figure 2), that implies a different physical structure. Fernández-Martín et al. (2012) describe a simple morphology for NGC 6888 where an ellipsoidal cavity has been carved inside the almost spherical outer optical shell. We can estimate lower and upper limits of the electron density of the X-ray-emitting gas by adopting spherical and ellipsoidal geometries, respectively. For the spherical model, we have adopted a radius of  $9'$  to obtain an rms electron density of  $n_e = 0.4(\epsilon/0.1)^{-1/2}$  cm $^{-3}$ , implying a mass of the X-ray-emitting gas of  $m_X = 1.7(\epsilon/0.1)^{1/2} M_\odot$ , where  $\epsilon$  is the gas filling factor. For the ellipsoidal case, we have assumed semiaxes of  $9'$ ,  $6'$ , and  $6'$  to obtain an rms electron density of  $n_e = 0.6(\epsilon/0.1)^{-1/2}$  cm $^{-3}$  and a mass of the X-ray-emitting gas of  $m_X = 1.2(\epsilon/0.1)^{1/2} M_\odot$ .

## 5. DISCUSSION

### 5.1. Comparison with previous X-ray studies

All previous X-ray analyses of the diffuse X-ray emission from NGC 6888 agree on the presence of a main plasma component with a temperature  $\simeq 1.4 \times 10^6$  K consistent with that reported in our analysis of the *Chandra* ACIS data. As for the hot component, there are notable discrepancies: Wrigge et al. (1994) did not find evidence of this hot component using *ROSAT* PSPC data, Wrigge et al. (2005) found a hot component with a temperature marginally higher by  $\simeq 13\%$  than ours using *ASCA* SIS observations, and Zhekov & Park (2011) reported a second temperature component significantly hotter than ours,  $kT \geq 2$  keV, using *Suzaku* XIS data. The lack of hot component in the *ROSAT* PSPC data can be attributed to the low sensitivity of this instrument to energies above 1.0 keV. On the other hand, the high temperature for the secondary component reported by Zhekov & Park (2011) originated on the high level of X-ray emission in the range 1.5-4.0 keV found in the *Suzaku* XIS data. The lack of such a hard component in the spectra derived from the *Chandra* ACIS observations is in sharp contrast with the *Suzaku* XIS data. We present in Figure 6 the combined spectrum of point sources projected onto the nebula in the ACIS-S3 detector. The spectrum of the point sources is clearly harder than that of the nebula and shows significant emission above 0.8 keV up to 5-7 keV. Its count rate is  $0.0188 \sim 0.0005$  cnts s $^{-1}$ , i.e.,  $\sim 12\%$  that of the nebular ACIS-S3 region. This emission can be formally fitted using an absorbed model<sup>4</sup> comprising an optically-thin plasma emission component at a temperature of  $(7.7 \pm 1.0) \times 10^6$  K and a power-law component with photon index  $\Gamma = 1.16 \pm 0.08$

<sup>4</sup> For consistency with the spectral fit of the nebular emission from NGC 6888, we have adopted a hydrogen column density of  $3.1 \times 10^{21}$  cm $^{-2}$ .

TABLE 1  
SPECTRAL FITS OF THE DIFFUSE X-RAY EMISSION FROM NGC 6888

Region	Counts	$X_N$	$kT_1$ (keV)	$A_1$ (cm $^{-5}$ )	$f_1$ (erg cm $^{-2}$ s $^{-1}$ )	$F_1$ (erg cm $^{-2}$ s $^{-1}$ )	$kT_2$ (keV)	$A_2$ (cm $^{-5}$ )	$f_2$ (erg cm $^{-2}$ s $^{-1}$ )	$F_2$ (erg cm $^{-2}$ s $^{-1}$ )	$F_1/F_2$	$\chi^2/\text{DoF}$
CCID S3	14000 $\pm$ 250	5.3 $^{+0.7}_{-0.7}$	0.140 $^{+0.003}_{-0.003}$	6.1 $\times 10^{-3}$	4.7 $\times 10^{-13}$	7.5 $\times 10^{-12}$	0.67 $^{+0.04}_{-0.03}$	1.7 $\times 10^{-4}$	1.7 $\times 10^{-13}$	5.2 $\times 10^{-13}$	14.4	1.5=170.3/109
A1	10250 $\pm$ 200	5.3 $^{+0.9}_{-0.9}$	0.140 $^{+0.008}_{-0.005}$	3.9 $\times 10^{-3}$	3.2 $\times 10^{-13}$	5.0 $\times 10^{-12}$	0.68 $^{+0.05}_{-0.05}$	1.2 $\times 10^{-4}$	1.2 $\times 10^{-13}$	3.7 $\times 10^{-13}$	13.6	1.6=173.5/105
B1	3300 $\pm$ 120	3.7 $^{+1.3}_{-1.0}$	0.117 $^{+0.012}_{-0.007}$	3.2 $\times 10^{-3}$	1.2 $\times 10^{-13}$	2.5 $\times 10^{-12}$	0.66 $^{+0.08}_{-0.09}$	3.9 $\times 10^{-5}$	3.9 $\times 10^{-14}$	1.2 $\times 10^{-13}$	20.7	1.1=93.0/89
CCID S4	4700 $\pm$ 350	5.0	0.101 $^{+0.008}_{-0.008}$	2.7 $\times 10^{-2}$	7.0 $\times 10^{-13}$	1.5 $\times 10^{-11}$	0.64 $^{+0.07}_{-0.07}$	1.8 $\times 10^{-4}$	1.8 $\times 10^{-13}$	4.7 $\times 10^{-13}$	30.9	1.5=136.6/90
A2	3200 $\pm$ 150	5.0	0.100 $^{+0.018}_{-0.008}$	2.2 $\times 10^{-2}$	5.5 $\times 10^{-13}$	1.4 $\times 10^{-11}$	0.64 $^{+0.08}_{-0.08}$	1.4 $\times 10^{-4}$	1.3 $\times 10^{-13}$	4.2 $\times 10^{-13}$	34.5	1.9=115.9/59
B2	1550 $\pm$ 100	5.0	0.118 $^{+0.043}_{-0.004}$	3.4 $\times 10^{-3}$	1.5 $\times 10^{-13}$	3.1 $\times 10^{-12}$	0.65	3.8 $\times 10^{-5}$	3.8 $\times 10^{-14}$	1.2 $\times 10^{-13}$	25.7	0.6=20.13/31
CCID S34	...	4.0 $^{+0.5}_{-0.6}$	0.118 $^{+0.043}_{-0.004}$	3.1 $\times 10^{-2}$	1.1 $\times 10^{-12}$	2.4 $\times 10^{-11}$	0.64 $^{+0.04}_{-0.03}$	3.6 $\times 10^{-4}$	3.5 $\times 10^{-13}$	1.1 $\times 10^{-12}$	22.2	1.5=308.1/196

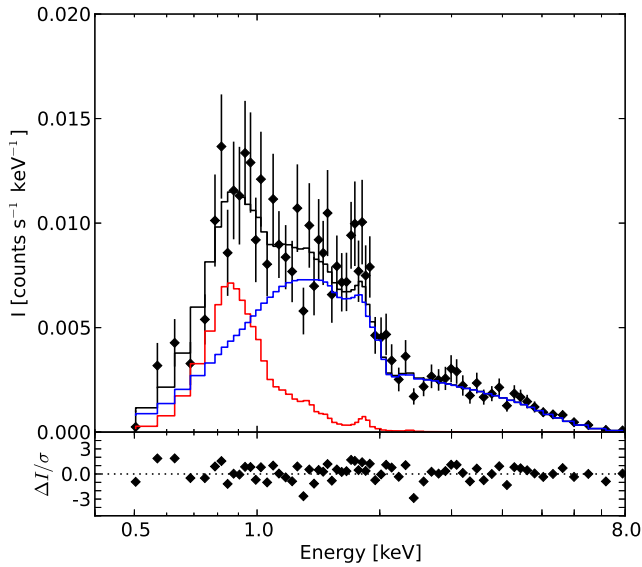


FIG. 6.— (top panel) Background-subtracted spectrum of point sources projected onto the nebula NGC 6888 in the *Chandra* ACIS-S3 detector overplotted with the best-fit model (black histogram) consisting of an absorbed *apec* (red histogram) and a power law (blue histogram) model. See text for details. (Bottom panel) Residuals of the spectral fit.

for a reduced  $\chi^2$  of  $62.30/63=0.99$ . The flux of this emission in the 0.3-2.0 keV is  $(4.1\pm 0.3)\times 10^{-14}$  erg cm $^{-2}$  s $^{-1}$ , i.e., it accounts for 6% of the nebular flux measured in the ACIS-S3 spectrum in this band. The total flux in the 0.3-9.0 keV of this component is  $(2.46\pm 0.24)\times 10^{-13}$  erg cm $^{-2}$  s $^{-1}$ . These results demonstrate that the hard, 1.5-4.0 keV component detected by *Suzaku* is an observational artifact caused by its limited spatial resolution ( $\sim 2'$ ), which makes difficult to identify point sources in the field of view of NGC 6888 and to excise their contribution from the diffuse emission.

The first observations of the X-ray emission toward NGC 6888 reported absorbed fluxes  $\sim 10^{-12}$  erg cm $^{-2}$  s $^{-1}$  (e.g., Bochkarev 1988; Wrigge et al. 1994, 2005) that were raised up to  $\sim 2\times 10^{-12}$  erg cm $^{-2}$  s $^{-1}$  by the more recent *Suzaku*'s observations (Zhekov & Park 2011). Our estimate for the observed flux ( $2.4\times 10^{-12}$  erg cm $^{-2}$  s $^{-1}$ ) is in good agreement with the latest measurements despite that a fraction of the nebula was not registered by the ACIS-S detectors and we had to rely on *ROSAT* PSPC observations to estimate the total flux. Sensitive observations with a large field of view, as those that would be provided by *XMM-Newton*, are most needed to search for the fainter and more extended X-ray emission in this WR nebula.

Our *Chandra* ACIS-S observation yielded the detection of three peaks in the spatial distribution of the diffuse X-ray emission in NGC 6888: two associated with the caps, and another one toward the NW blowout at the western edge of the ACIS-S field of view in CCD S4. The latter peak in the X-ray emission is hinted in *ROSAT* PSPC and HRI, and *ASCA* SIS observations (Wrigge et al. 1994; Wrigge & Wendker 2002; Wrigge et al. 2005), but it has not been reported previously to be part of the X-

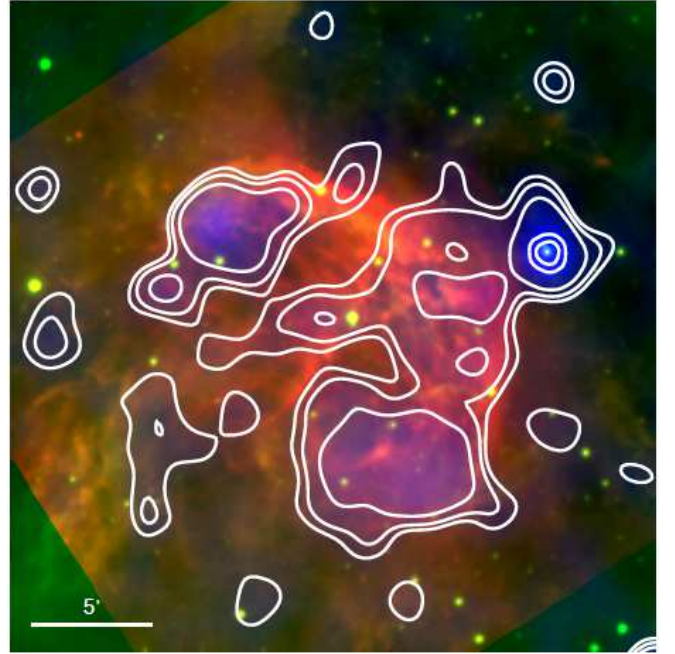


FIG. 7.— *Spitzer* MIPS 24  $\mu$ m (red), *WISE* 12  $\mu$ m (green), and *ROSAT* PSPC (blue and contours) colour-composite picture of NGC 6888.

ray-emitting gas associated with the nebula<sup>5</sup>. This additional emission component is located in a region with no H $\alpha$  counterpart (see Figure 2; Gruendl et al. 2000), but it is spatially delineated by the [O III] outer shell. The situation is reminiscent of the northwest blowout in S 308, which can be ascribed to the action of the hot gas carving a cavity towards a low density region of the circumstellar medium (CSM; Chu et al. 2003; Toalá et al. 2012).

In contrast to the limb-brightened morphology of the X-ray-emitting gas reported for S 308 (Toalá et al. 2012), the current (and previous) X-ray observations of NGC 6888 do not show such a simple morphology, but that the hot gas is distributed in (at least) three maxima. The comparison between infrared images of NGC 6888 and that obtained by *ROSAT* PSPC of the X-ray-emitting gas (see Figure 6) is suggestive of a correlation between the regions where the X-ray emission is faintest, toward the southeast region of NGC 6888, and a molecular filament traced in infrared wavelengths. Spatial variations of the amount of intervening material across the nebula, not accounted so far, can be playing an interesting role in the X-ray morphology of NGC 6888.

Finally, it is worth mentioning here that the apparent nitrogen overabundances are still consistent with the values reported by Fernández-Martín et al. (2012) in their region X1. This region is spatially coincident with one of the brightest clumps in the X-ray-emitting region.

## 5.2. Comparison with simulations

There have been several attempts in the past to model the morphology and X-ray emission from NGC 6888 revealed by *ROSAT*, *ASCA*, and *Suzaku* observations.

<sup>5</sup> The *Suzaku* observations did not map this nebular region, which was not registered by its detectors.

One-dimensional (1D) analytic or hydrodynamic models are an elegant first approximation to the evolution of the CSM of WR stars (e.g., Zhekov & Myasnikov 1998), although they do not include the effects of ionization due to the central star, neither can they reproduce the wealth of structures produced by hydrodynamical instabilities, which seem to trace the X-ray-emitting gas in some regions inside the bubble. Furthermore, those simulations are not able to reproduce simultaneously regions in which instabilities are important (e.g., the caps) and regions where there are no clumps (the blowout). García-Segura et al. (1996) presented 2D hydrodynamical simulations of the evolving medium around a star with an initial mass of  $35 M_{\odot}$ . The broad morphological properties of NGC 6888 could be reproduced adopting a slow RSG wind of  $15 \text{ km s}^{-1}$ . These simulations were refined by Freyer et al. (2006) who included the effects of photoionization. Despite the progress achieved by the 2D radiative hydrodynamic models published to date, which have helped us advance our understanding of the formation of NGC 6888, they fail to produce blowout-like features. Blowouts might result from anisotropies in the RSG or non uniformities in the interstellar medium. Simulations recently presented by Rogers & Pittard (2013) explore the evolution of a non uniform initial interstellar medium around massive stars. Specific modeling accounting for these features are needed to understand the morphology and distribution of the X-ray-emitting gas in NGC 6888.

It is often argued that thermal conduction between the cold ( $10^4 \text{ K}$ ) outer RSG material and the inner hot ( $10^7 - 10^8 \text{ K}$ ) bubble causes the temperature of the hot bubble to drop to the observed values of  $T_X \sim 10^6 \text{ K}$  (e.g., Zhekov & Myasnikov 1998; Arthur 2007; Pittard 2007). Toalá & Arthur (2011) recently presented numerical models including conductive effects (classical and saturated thermal conduction) of WR bubbles that result in a wide range of temperatures capable of generating the soft X-ray emission observed in NGC 6888. Indeed, they present a spectrum corresponding to a nitrogen-rich plasma that shows two main components, one at  $0.5 \text{ keV}$  and another at  $\sim 0.9 \text{ keV}$ , very similar to the spectra presented in Figure 4 (see also Dwarkadas & Rosenberg 2013, for a comparison with models without thermal conduction).

Finally, it is interesting to check whether the central star of NGC 6888 can provide the observed X-ray-emitting material. García-Segura et al. (1996) could match the morphology of their 2D simulations with that of NGC 6888 at a time  $\sim 12,000 \text{ yr}$  after the onset of the WR phase. That time-lapse is further reduced to  $\sim 8,000 \text{ yr}$  when the dynamical effects on the nebular material of the photoionization are accounted (Freyer et al. 2006). For a mass-loss rate of  $3.1 \times 10^{-5} M_{\odot} \text{ yr}^{-1}$  (Abbott et al. 1986), the total mass provided by the star amounts up to  $0.25 - 0.37 M_{\odot}$ , which is smaller than the estimate of  $>1 M_{\odot}$  for the mass of hot plasma inside NGC 6888. Apparently, the WR wind has not had sufficient time to inject all the hot gas inside NGC 6888. This supports the possibility that physical processes such as thermal conduction have transferred material from the outer RSG shell into the hot bubble. The enhanced N/O ratio of the hot plasma, similar to that measured in the

cold shell through optical emission lines, is in concordance with this possibility.

## 6. SUMMARY AND CONCLUSIONS

We present *Chandra* ACIS-S observations of the NE quadrant and western regions of NGC 6888. We have used these observations to study the spatial distribution of the diffuse X-ray emission inside the nebula and derived global values of its physical conditions. In particular we find:

- The hot gas in NGC 6888 is distributed inside the optical shell delineated by [O III] emission. The spatial distribution of the X-ray emission shows enhancements towards the caps and a blowout present in the NW region of NGC 6888. This blowout, not discussed in previous studies, has no H $\alpha$  counterpart, but an outer *skin* of [O III] is detected. The X-ray-emitting gas is, thus, traced by H $\alpha$  clumps inside the nebular shell and by the blowout. No clear evidence of limb-brightening is detected.
- The X-ray emission is dominated by the N VII  $0.5 \text{ keV}$  line with additional contributions of the Fe complex and Ne IX line at  $0.7 - 0.9 \text{ keV}$ . The spectrum declines with energy, fading at energies higher than  $1.5 \text{ keV}$ . The X-ray emission from NGC 6888 can be described by a two-temperature optically thin plasma emission model with temperatures of  $\sim 1.4 \times 10^6 \text{ K}$  and  $7.4 \times 10^6 \text{ K}$ .
- The intrinsic total flux emitted by NGC 6888 in the  $0.3 - 2 \text{ keV}$  energy band is estimated to be  $\sim (4.05 \pm 0.5) \times 10^{-11} \text{ erg cm}^{-2} \text{ s}^{-1}$ , and the X-ray luminosity at a distance of  $1.26 \text{ kpc}$  is  $L_X = (7.7 \pm 0.1) \times 10^{33} \text{ erg s}^{-1}$ .
- The estimated rms electron density  $n_e$  of the X-ray-emitting gas ranges between  $0.4 \times (\epsilon/0.1)^{-1/2}$  and  $0.6 \times (\epsilon/0.1)^{-1/2} \text{ cm}^{-3}$  resulting in an estimated total mass of  $1.7 \times (\epsilon/0.1)^{1/2} M_{\odot}$  and  $1.2 \times (\epsilon/0.1)^{1/2} M_{\odot}$ , respectively. The density, temperature, and abundance of the X-ray-emitting gas are consistent with the expectation of thermal conduction at the wind-wind interaction zone, where the RSG wind material is mixed in the shocked WR wind in the bubble interior.

Future *XMM-Newton* observations are needed to acquire a complete view of the soft X-ray emission from the hot plasma in NGC 6888 with better spatial coverage, sensitivity, and energy resolution than the existing studies. As the blowout detected in NGC 6888 is at the edge of the cameras of the ACIS-S instrument and a significant section of the bubble remains unobserved, *XMM-Newton* observations could finally unveil the total distribution of the hot gas in this nebula. The soft sensitivity and spatial coverage of such observations would also be very valuable to assess the varying amounts of intervening material across the nebula suggested by optical and infrared observations.



We want to thank the anonymous referee for her/his comments that improved the presentation of the technical details in this paper. This work is funded by grants NASA *Chandra* X-ray observatory Guest Observer Program Grant SAO G03-4023X, and AYA 2005-01495 of the Spanish MEC (Ministerio de Educación y Ciencia) and

AYA 2011-29754-C03-02 of the Spanish MICINN (Ministerio de Ciencia e Innovación) co-funded with FEDER funds. JAT also acknowledges support by the CSIC JAE-Pre student grant 2011-00189. JAT is grateful to Y. Jiménez-Teja for introducing him to the use of matplotlib routines.

## REFERENCES

- Abbott, D. C., Beiging, J. H., Churchwell, E., & Torres, A. V. 1986, *ApJ*, 303, 239
- Anders, E., & Grevesse, N. 1989, *Geochim. Cosmochim. Acta*, 53, 197
- Arnaud, K. A. 1996, *Astronomical Data Analysis Software and Systems V*, 101, 17
- Arthur, S. J. 2007, *Diffuse Matter from Star Forming Regions to Active Galaxies*, 183
- Balucińska-Church, M., & McCammon, D. 1992, *ApJ*, 400, 699
- Bochkarev, N. G. 1988, *Nature*, 332, 518
- Chu, Y.-H., Troland, T. H., Gull, T. R., Treffers, R. R., & Kwitter, K. B. 1982, *ApJ*, 254, 562
- Chu, Y.-H., Treffers, R. R., & Kwitter, K. B. 1983, *ApJS*, 53, 937
- Chu, Y.-H., Guerrero, M. A., Gruendl, R. A., García-Segura, G., & Wendker, H. J. 2003, *ApJ*, 599, 1189
- Chu, Y.-H., Gruendl, R. A., & Guerrero, M. A. 2006, *The X-ray Universe 2005*, 604, 363
- Chu, Y.-H. 2008, *IAU Symposium*, 250, 341
- Dwarkadas, V. V., & Rosenberg, D. L. 2013, *High Energy Density Physics*, 9, 226
- Fernández-Martín, A., Martín-Gordón, D., Vílchez, J. M., et al. 2012, *A&A*, 541, A119
- García-Segura, G., & Mac Low, M.-M. 1995, *ApJ*, 455, 145
- García-Segura, G., Langer, N., & Mac Low, M.-M. 1996, *A&A*, 316, 133
- Gosset, E., Nazé, Y., Claeskens, J.-F., et al. 2005, *A&A*, 429, 685
- Gruendl, R. A., Chu, Y.-H., Dunne, B. C., & Points, S. D. 2000, *AJ*, 120, 2670
- Freyer, T., Hensler, G., & Yorke, H. W. 2006, *ApJ*, 638, 262
- Hamann, W.-R., Wessolowski, U., & Koesterke, L. 1994, *A&A*, 281, 184
- Humphreys, R. M. 2010, *Hot and Cool: Bridging Gaps in Massive Star Evolution*, 425, 247
- Johnson, H. M., & Hogg, D. E. 1965, *ApJ*, 142, 1033
- Meynet, G., & Maeder, A. 2003, *A&A*, 404, 975
- Moore, B. D., Hester, J. J., & Scowen, P. A. 2000, *AJ*, 119, 2991
- Pittard, J. M. 2007, *Diffuse Matter from Star Forming Regions to Active Galaxies*, 245
- Rogers, H., & Pittard, J. M. 2013, *MNRAS*, 431, 1337
- Sharpless, S. 1959, *ApJS*, 4, 257
- Snowden, S. L., Egger, R., Freyberg, M. J., et al. 1997, *ApJ*, 485, 125
- Toalá, J. A., & Arthur, S. J. 2011, *ApJ*, 737, 100
- Toalá, J. A., Guerrero, M. A., Chu, Y.-H., et al. 2012, *ApJ*, 755, 77
- van der Hucht, K. A. 2001, *New A Rev.*, 45, 135
- Wendker, H. J., Smith, L. F., Israel, F. P., Habing, H. J., & Dickel, H. R. 1975, *A&A*, 42, 173
- Wrigge, M., Wendker, H. J., & Wisotzki, L. 1994, *A&A*, 286, 219
- Wrigge, M., Chu, Y.-H., Magnier, E. A., & Kamata, Y. 1998, *IAU Colloq. 166: The Local Bubble and Beyond*, 506, 425
- Wrigge, M. 1999, *A&A*, 343, 599
- Wrigge, M., & Wendker, H. J. 2002, *A&A*, 391, 287
- Wrigge, M., Chu, Y.-H., Magnier, E. A., & Wendker, H. J. 2005, *ApJ*, 633, 248
- Zhekov, S. A., & Myasnikov, A. V. 1998, *New A.*, 3, 57
- Zhekov, S. A., & Park, S. 2011, *ApJ*, 728, 135